Epitaxial Bi$_5$Ti$_3$FeO$_{15}$−CoFe$_2$O$_4$ Pillar−Matrix Multiferroic Nanostructures

Akira Imai,[†,‡,□] Xuan Cheng,[‡,□] Huolin L. Xin,[§] Eugene A. Eliseev,[⊥] Anna N. Morozovska,[⊥] Sergei V. Kalinin,[∥] Ryota Takahashi,[#] Mikk Lippmaa,[#] Yuji Matsumoto,[†,△,*] and Valanoor Nagarajan[‡]

[†]Materials and Structures Laboratory, Tokyo Institute of Technology, 4259 Nagatsuta, Midori-ku Yokohama 226-8503, Japan, [‡]School of Materials Science and Engineering, University of New South Wales, Sydney, NSW 2052, Australia, [§]Center for Functional Nanomaterials, Brookhaven National Laboratory, Upton, New York 11973, United States, [⊥]Institute of Physics, Institute for Problems of Material Sciences, National Academy of Sciences of Ukraine, 03028 Kiev, Ukraine, [∥]The Center for Nanophase Materials Sciences, Oak Ridge National Laboratory, Oak Ridge, Tennessee 37831, United States, [#]Institute for Solid State Physics, University of Tokyo, Kashiwanoha 5-1-5, Kashiwa, Chiba 277-8581, Japan, and [△]Department of Applied Chemistry, School of Engineering, Tohoku University, 6-6-07 Aramaki Aza Aoba, Aoba-ku Sendai, 980-8579 Japan. [□]A. Imai and X. Cheng contributed equally to the work.

ABSTRACT
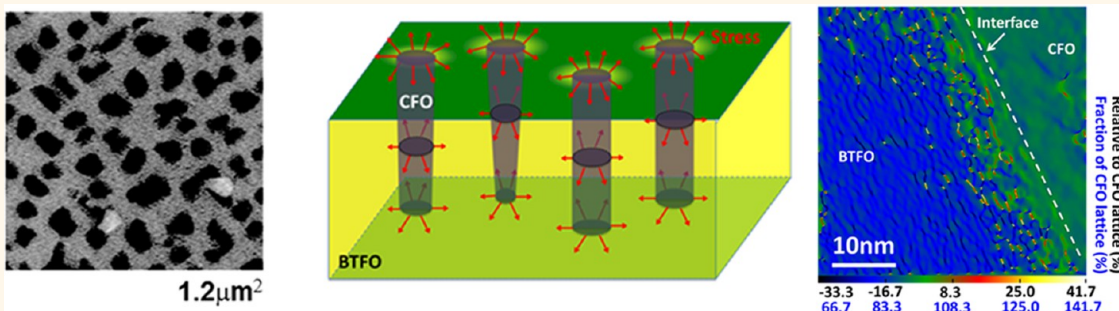
Epitaxial self-assembled ferro(i)magnetic spinel (CoFe$_2$O$_4$ (CFO)) and ferroelectric bismuth layered perovskite (Bi$_5$Ti$_3$FeO$_{15}$ (BTFO)) pillar−matrix nanostructures are demonstrated on (001) single-crystalline strontium titanate substrates. The CFO remains embedded in the BTFO matrix as vertical pillars ($\sim$50 nm in diameter) up to a volume fraction of 50%. Piezoresponse force microscopy experiments evidence a weak out-of-plane and a strong in-plane ferroelectricity in the BTFO phase, despite previously reported paraelectricity along the *c*-axis in a pure BTFO film. Phenomenological Landau−Ginzburg−Devonshire-based thermodynamic computations show that the radial stress induced by the CFO nanopillars can influence these ferroelectric phases, thus signifying the importance of the nanopillars. The CFO pillars demonstrate robust ferromagnetic hysteresis loops with little degradation in the saturation magnetization (*ca.* 4 μ_B/f.u.). Thus BTFO−CFO nanocomposites show significant promise as a lead-free magnetoelectric materials system.

KEYWORDS: oxide film · pulsed laser deposition · nanocomposite · PFM

I n the past decade there has been significant interest in the design and development of pillar-and-matrix nanocomposite oxide materials for functional applications.[1−4] One class of oxide materials where this approach has been very effective is multiferroic systems.[2,5−7] This is primarily triggered by the paucity of truly single-phase multiferroics that show strong ferroelectric and ferromagnetic properties simultaneously, particularly at temperatures appealing for devices.[8−11] Furthermore such nanocomposite multiferroics systems allow epitaxial strain and substrate orientation effects to be exploited in order to achieve accurate control over shape, density, and dimensions of the nanopillars.[12,13] Combinations of ferroelectric (FE) and ferro(i)magnetic (FM) oxides in epitaxial nanocomposites also allow mutual controllability through the elastic coupling interactions across the FE−FM interface.
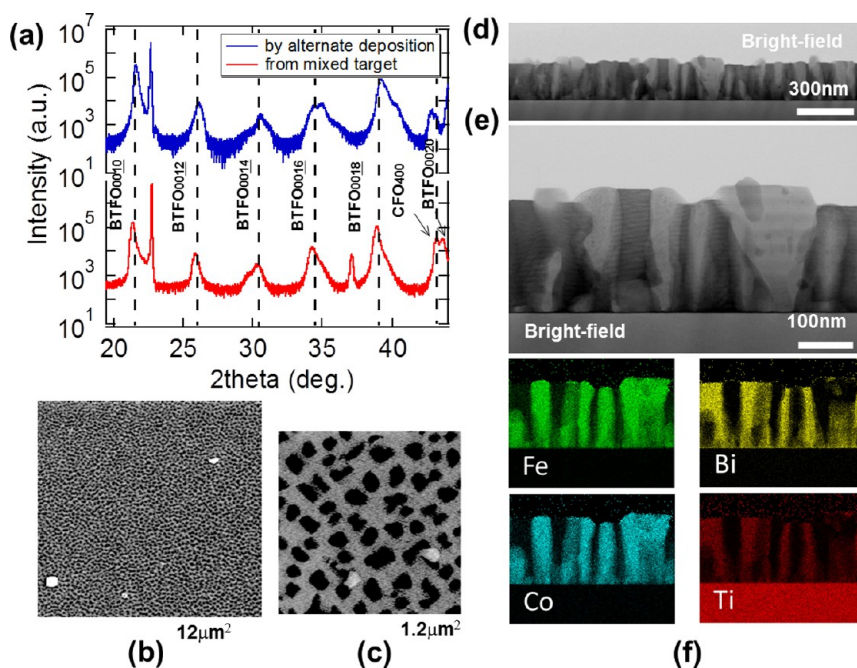
In systems that have been popular thus far, the FM material is chosen from the AB$_2$O$_4$ spinel family (such as CoFe$_2$O$_4$ or NiFe$_2$O$_4$) and the FE material is chosen from ABO$_3$ "simple cubic" perovskites (such as

Figure 1. (a) XRD patterns of BTFO—CFO thin films *via* simultaneous deposition (red) and alternating deposition (blue). (b and c) SEM images showing that CFO is well dispersed in the BTFO matrix throughout the entire sample. (d and e) BFTEM images showing that the nanopillars grow vertically to the bottom of the matrix. (f) EDS revealing the elemental composition of both nanopillars and matrix.

$BaTiO_3$, $PbTiO_3$, and $BiFeO_3$), respectively. The two constituent materials selected are such that they are immiscible at the growth temperatures in order to promote the two-phase nucleation and a clean interface between the pillar and the matrix. For further development of new multiferroic epitaxial nanocomposites bismuth-layer-structured ferroelectrics (BLSFs) demonstrate significant potential. BLSFs are (i) lead-free and hence environmentally friendly, (ii) show robust polarization values commensurate to most lead-based ferroelectrics, and (iii) have been shown to be virtually resistant to polarization fatigue.[14,15] In addition to this, since the BLSF materials have a strong anisotropy in the spontaneous polarization, they offer the unique opportunity to tailor the ferroelectric polarization by means of an epitaxial strain at the two-phase boundary. Despite these well-known features, BSLFs have not attracted attention as candidates for such nanocomposite systems.

At the same time there is an unanswered question: can the strain induced by the pillar phase induce new types of ferroic order parameters? For example, can the local radial strain imposed by the nanopillars induce ferroelectric polarization along crystallographic directions that would normally not exhibit any polar properties in the corresponding bulk phase? If this can be shown, then an entirely unexplored pathway of making ferroelectrics, namely, exploiting local strain from inclusions, can be developed. This would complement current ideologies, such as either tuning the bulk composition or using epitaxial strain, that are commonly employed to develop new ferroelectrics.

In this study we report the synthesis of a new lead-free multiferroic nanocomposite. The matrix is composed of a BSLF FE material, bismuth iron titanate with the chemical formula $Bi_5Ti_3FeO_{15}$ (BTFO), and the pillars are the FM component composed of the well-known ferromagnetic spinel cobalt ferrite ($CoFe_2O_4$: CFO). The nanocomposite is synthesized on (001) oriented $SrTiO_3$ single-crystal substrates *via* a combinatorial pulsed laser deposition technique. It is shown that the density of the pillars can be systematically controlled by the volume fraction of CFO deposited. The radial stress induced by the CFO nanopillars is found to be sufficient to induce a weak out-of-plane polarization in the BTFO matrix and a very strong in-plane polarization component, as detected by piezo-response force microscopy. This is distinctly absent in BTFO thin films of comparable thickness, thus signifying the importance of the nanopillars. The magnetic measurements for BTFO and BTFO/CFO nanocomposite films show that most magnetization arises from CFO nanopillars with little degradation of the saturation magnetization.

RESULTS AND DISCUSSION

Figure 1a is a typical set of X-ray diffraction (XRD) patterns of the BIT—CFO nanocomposite films obtained either by depositing BIT and CFO simultaneously from a single mixed target of BIT—CFO (30 vol % CFO) or by alternating pure BIT and CFO targets such that the nominal CFO composition was 40 vol %. These two XRD patterns are almost identical to each other. They both
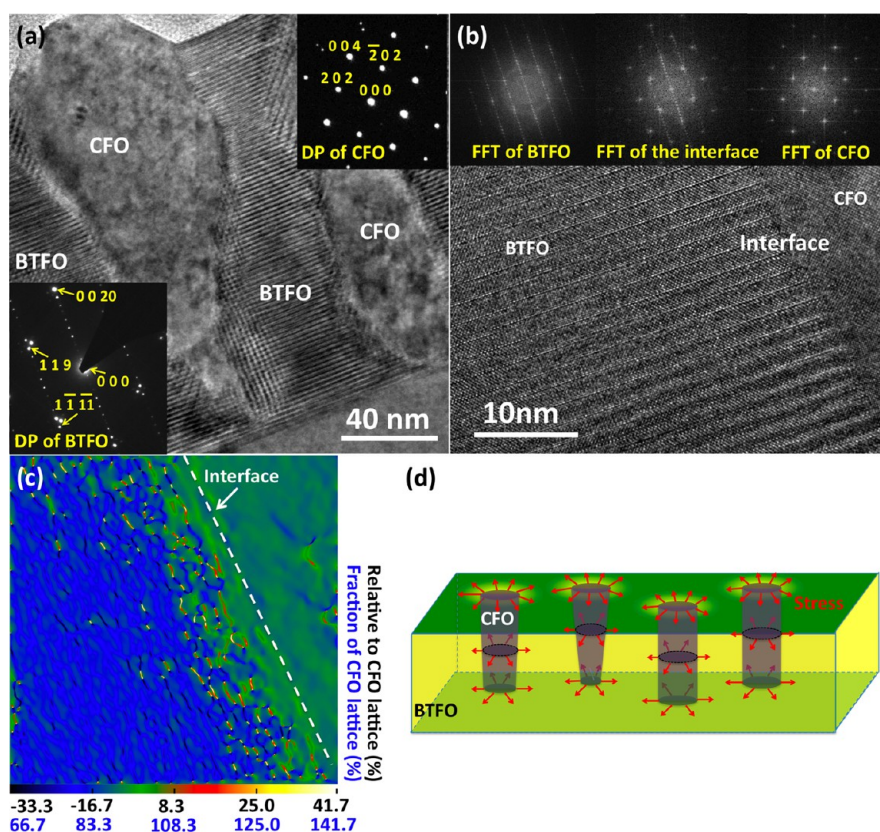
Figure 2. (a) HRTEM image of the CFO pillar in BTFO matrix with SAED of BTFO matrix (inset bottom left) and CFO pillar (inset top right) showing the crystallography and the epitaxial relationship between BTFO and CFO. (b) HRTEM image (obtained from a different region from part a) showing the interface between BTFO and CFO. The insets show the FFT images from BTFO, the interface, and CFO, respectively. (c) GPA of the HRTEM image in part b. (d) Schematic explaining how the radial stresses induce the coupling.

indicate the presence of the CFO phase growing with (001) out-of-plane orientation. Most interestingly they confirm the formation of a new single phase different from BIT. This is identified to be $Bi_5Ti_3FeO_{15}$ (BTFO) growing with (001) out-of-plane orientation. Scanning electron microscopy (SEM) analysis (Figure 1b) confirms the pillar—matrix nanocomposite to grow over the entire sample surface area. Figure 1c is a high-magnification SEM image that reveals the nanopillars (∼50 nm in average width) as dark areas embedded in a bright(er) matrix phase. The morphology is very similar to previously reported vertical nanopillar nano-composites structures.[1,16,17] Bright-field transmission electron microscope (TEM) images (Figure 1d and e) clearly confirm that the nanopillars run right to the substrate, although the walls are not perfectly vertical. To identify the chemical composition of the nanopillars vis-à-vis the matrix, cross-section TEM-EDX (energy-dispersive X-ray spectroscopy) analysis was carried out. The chemical EDS analysis maps (Figure 1f) reveal the nanopillars are CFO and the matrix is BTFO.

The results from the structural characterization experiments reveal that some of Fe atoms from the CFO phase get incorporated into the BIT lattice to form the BTFO phase. This happens irrespective of the manner

of deposition (i.e., either co-deposition of CFO and BIT or alternate deposition of each component) on Nb: STO. However, it is noted that this is not a stoichiometric reaction, and hence some excess Co and/or Ti atoms as the result of the BTFO phase formation must be precipitated. In fact, some precipitates were indeed found on the surface, as shown in SEM images of Figure 1b and c, although no impurity phase was detected by either XRD or TEM. Nevertheless, the nanocomposite structure can be controlled. For example, the density of the CFO pillars increases linearly as the starting ratio of CFO increases up to 50 vol % with the size of nanopillars remaining unchanged (Figure S1). Note that the same BTFO—CFO nanopillar—matrix structure could be also obtained even starting from BTFO and CFO targets, which indicates that the nanopillar composite structure is the most stable phase under the presented growth conditions.

High-resolution TEM (HRTEM) was then carried out to investigate the nature of the interface separating the two phases as well as identify the epitaxial relationships of the two-phase sample. The selective area electron diffraction (SAED) patterns of BTFO and CFO (see Figure 2a insets) from Figure 2a show the crystallography of BTFO and CFO, respectively. They agree
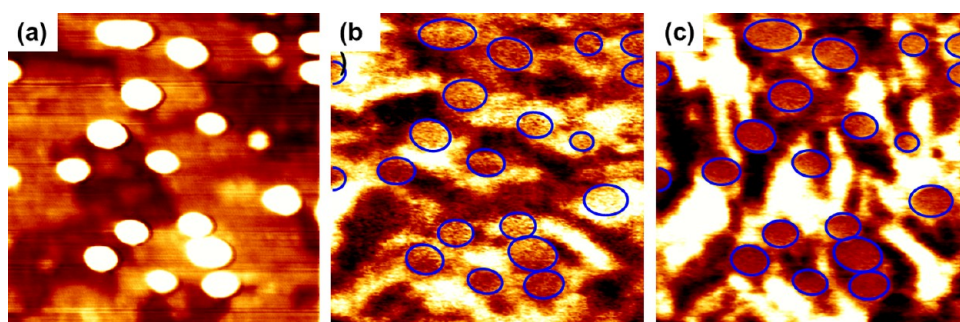
Figure 3. Simultaneously acquired PFM images of BTFO—CFO (23 vol % CFO) sample (1 × 1 μm^2 area). (a) Topography images with nanopillars shown in white color. (b) OPP image showing weak signals for both nanopillars (marked by yellow circles) and matrix. (c) IPP image showing zero contrast for the nanopillars (marked by yellow circles) and strong contrast for the matrix.

with the fast Fourier transform (FFT) images (inset to Figure 2b) obtained from local regions *via* ImageJ software, thus confirming that the SAED patterns capture the local lattice arrangements without complications arising from multiple layers or neighboring phases. Distinct and clear diffraction spot reflections are observed for both SAED patterns, confirming that the BTFO and CFO are both single crystalline. As a [001] oriented STO substrate was used, the epitaxial relationship between the thin film and the substrate can be determined by indexing the SAED patterns. The epitaxial relationships of BTFO and CFO with respect to the STO substrate are as follows:

$$BTFO[110]//STO[100]([010])$$
$$CFO[100]//STO[100]([010])$$

Figure 2b is a high-resolution image of the BTFO—CFO interface. The long stacking structure of the layered perovskite of BTFO along the *c*-axis can be clearly observed from this image. The *c*-axis lattice parameter of BTFO measured from HRTEM is approximately 4.11 ± 0.1 nm, in good agreement with JCPDS (082-0063) data. Reciprocal space mapping of the BTFO—CFO composite film (not shown) revealed that the lattice constants, both in-plane and out-of-plane, of the matrix (0.385 nm in pseudocubic (pc) notation and 4.11 nm) and pillars (0.418 nm in pc notation) are nearly relaxed and close to those of the corresponding bulk. The lattice mismatch between BTFO and CFO for the in-plane (8.15%) and the out-of-plane (1.93%) is large enough to drive the nucleation of many misfit dislocations along the tubular interface, as is confirmed by TEM, discussed next.

In order to further understand the nature of the interface as well as map the local strain between the BTFO matrix and CFO nanopillars, geometric phase analysis (GPA)[18] was carried out. Full details are given in Supporting Information S2. The GPA analysis for a typical CFO—BTFO interface is shown in Figure 2c. The scale bar shows changes in the lattice spacing measured relative to the CFO pc *a*-axis parameter (0.418 nm). It reveals that the CFO—BTFO interface is

inhomogenously strained. However further away from the interface the BTFO relaxes to its bulk lattice parameter. GPA analysis of the BTFO/STO interface revealed that the BTFO is fully relaxed (Supporting Information S2) along the substrate interface. The inhomogenous strain close to the nanopillars along with the decay of strain from the tubular interface is one of the crucial features of this system. As will be discussed in the theory section, the local strain that stems from CFO nanopillars has significant influence on the stability of the ferroelectric polarization states. A schematic of this system is given in Figure 2d and further explained within the context of the pillar density dependence (Figure 4) and the theoretical model (Figure 5).

Piezoresponse force microscopy was then employed to investigate the ferroelectric domain and polarization switching properties of the film. Figure 3 shows the topography (a), out-of-plane piezoresponse (OPP) (b), and in-plane piezoresponse (IPP) images (1 × 1 μm^2 area) acquired simultaneously for a nanocomposite film with 23 vol % CFO. The nanopillars appear as white oval-shaped features in the topography image. Comparing the OPP and IPP images to the topography, we find that the nanopillars (marked by blue circles in the piezoresponse images) show zero (weak) signal. This reconfirms our assignation of the individual phases of the nanocomposite. CFO is a nonpolar material[19] and hence should appear as zero signal regions. On the other hand, the BTFO matrix shows (weak) OPP and (strong) IPP contrast. Nakashima *et al.* have investigated the ferroelectric D—E hysteresis loops of epitaxial BTFO films with different orientations.[20] They show that since BTFO is essentially a derivative of bismuth titanate (which has a layered ferroelectric structure), the polarization must primarily lie along the *a*—*b* plane and it is paraelectric along the *c*-axis. Indeed, when a pure BTFO film was examined by piezoresponse force microscopy (PFM), the ferroelectric domain structure was observed to lie purely in-plane along the *a*-axis and the OPP response showed zero signal (Figure S3). In contrast, for the BFTO—CFO nanocomposite in Figure 3 there is a clear OPP signal, although it is much weaker than the corresponding IPP
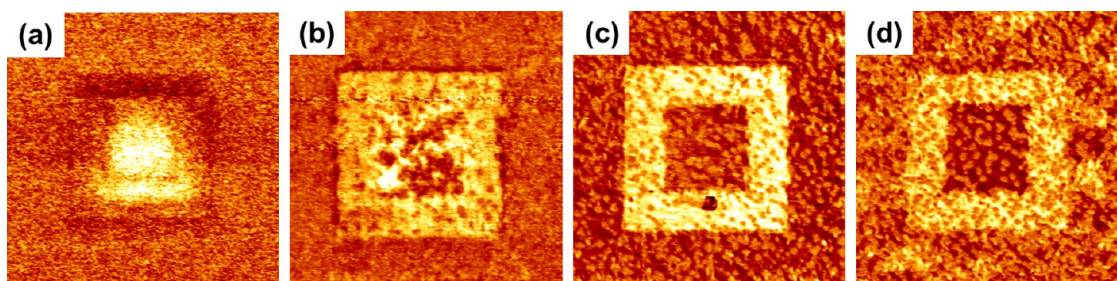
Figure 4. (a−d) IPP piezoresponse force microscopy (PFM) images for four compositions where the volume fraction of the CFO is systematically increased (a, 5%; b, 20%; c, 35%; and d, 45%). The square box domain pattern was written by scanning the PFM tip with +6 V bias over a $3 \times 3\ \mu m^2$ area followed by $1.5 \times 1.5\ \mu m^2$ area scan with the probe biased at −6 V. The panel confirms that the IPP PFM signal, as well as the contrast achieved, becomes stronger with increasing CFO pillar density, saturating at the 35% composition.

signal. The nanocomposite can be imagined to be equivalent to a BTFO film, which is penetrated by several CFO nanopillars. As already mentioned above, the lattice constants measured by XRD for both phases are almost relaxed, but the careful strain mapping by TEM indicates an inhomogeneous strain exists at the interface. This is the key part of the interaction mechanism: CFO nanopillars impose a local radial stress (see schematic of Figure 2d) that influences the ferroelectric domain switching behavior.

This is further explored in Figure 4a−d. We present IPP PFM images for four compositions where the volume fraction of the CFO is systematically increased (a, 5%; b, 20%; c, 35%; and d, 45%). The square box domain pattern was written by scanning the PFM tip with +6 V bias over a $3 \times 3\ \mu m^2$ area followed by $1.5 \times 1.5\ \mu m^2$ area scan with the probe biased at −6 V. The corresponding OPP images are given in Figure S4, and we find that there is an increasing (but still weak) OPP signal with increase in the nanopillar volume fraction. Most distinctly, as the volume fraction of the CFO pillars increases, the IPP signal as well as the contrast achieved becomes stronger, saturating at the 35% composition. For compositions with CFO greater than this volume fraction, the PFM signal deteriorated considerably, as now the CFO becomes the matrix and the BTFO constituent may begin to take the shape of nanopillars. This means that the phase stability of the polarization is affected dramatically around the nanopillars.

To understand how the presence of the nanopillars can create new polar phases with a polarization component along the a- and c-axes, thermodynamic Landau−Ginzburg−Devonshire (LGD) computations were carried out. LGD allows us to focus on the thermodynamic stability of local observations of ferroelectric nanodomain structures for both out-of-plane and in-plane polarization directions and their anisotropic behavior. The possibility to observe out-of-plane polarization direction in the BTFO matrix strained by CFO inclusions is revealed from a BTFO phase diagram, which is plotted in the coordinates of applied stress vs the favorable polarization direction. In actuality, quasi-cylindrical CFO inclusions primarily create

inhomogeneous in-plane radial stresses ($\sigma_{11} = \sigma_{22} = \sigma_{\rho\rho}$) inside the BTFO matrix. Approximate analytical expressions for inhomogeneous radial strains in the BTFO matrix due to the difference in thermal expansion coefficients ($\sigma_{\rho\rho}^t$) of cylindrical CFO inclusions of radius R and electrostriction effect in BTFO ($\sigma_{\rho\rho}^Q$) are fully developed in Supporting Information S5. It is very important that the stresses' decay obeys the power law outside the CFO inclusions, $\rho \geq R$,

$$\sigma_{\rho\rho}(\rho) = \sigma_{\rho\rho}^t(\rho) + \sigma_{\rho\rho}^Q(\rho) \propto (R/\rho)^2 \qquad (1)$$

That is, they must be long-range (see Figure 5a) and can create the stress-induced transition in the BTFO matrix. Quantitatively the stresses given by eq 1 readily reach relatively high values (up to several GPa). Depending on the sign of the stress and CFO inclusions concentration (volume fraction), the regions near the inclusions (or even far enough from the inclusions for larger volume fractions) can be under either compressive or tensile strain. As a result, either the in-plane (aa-phase, tensile strain) or out-of-plane (c-phase, compressive strain) polarization direction can become more favorable. Also the in-plane and out-of-plane aac-phase (mixed phase) can be favorable. One can expect that the polarization direction can be changed more strongly in the immediate vicinity of the inclusions, where the stress field changes are the highest. Analytical calculations of the BTFO phase diagram were performed within the Landau theory with material parameters listed in Supporting Information S5. As all Landau parameters for BTFO are unavailable, the simulations were performed using some of the material parameters corresponding to the Auruvilius compound of bismuth titanate ($Bi_4Ti_3O_{12}$, BIT), while other parameters were defined exactly for BTFO by fitting to available experimental results. In particular, the values of electrostriction Q_{ij} for BTFO were determined from the lattice constants' temperature dependences, namely, $a(T) = a_0(1 + Q_{11}P_{1S}^2(T))$, $b(T) = b_0(1 + Q_{21}P_{1S}^2(T))$, and $c(T) = c_0(1 + Q_{31}P_{1S}^2(T))$ available from refs 21 and 20. P_{1S} is the spontaneous polarization component. Below we also compare the results for BTFO and BIT.
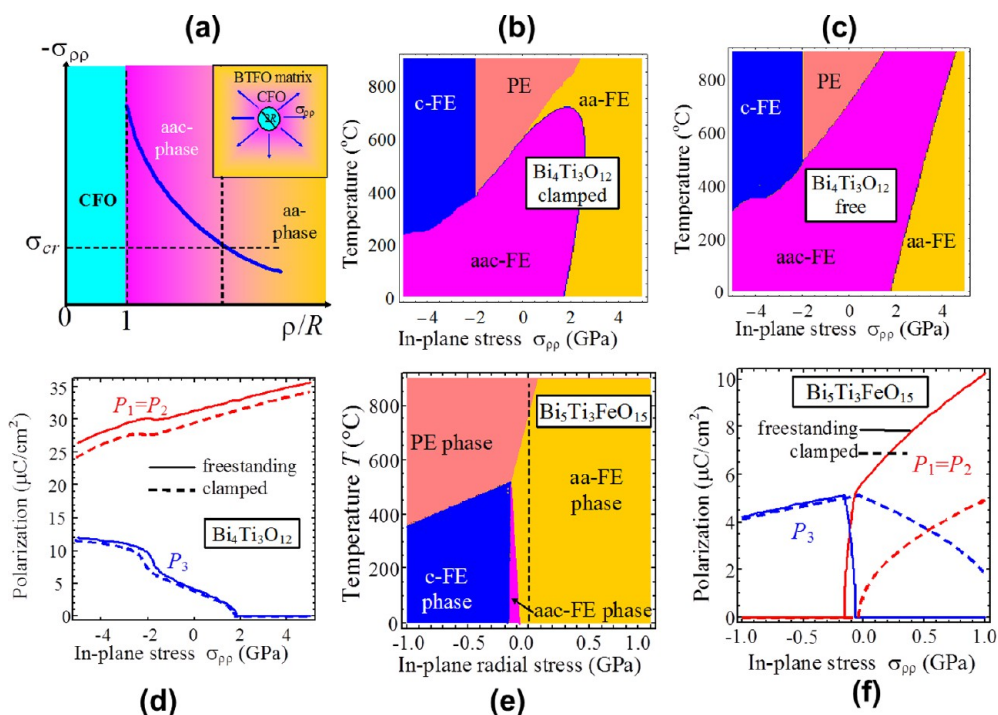
Figure 5. (a) Radial stress of BTFO matrix in dependence on the distance from the CFO inclusion. Inset: Scheme of CFO inclusion that "pushes away" the BTFO matrix in the radial direction, creating its compression, and (b) phase diagram of BIT film clamped on a rigid substrate calculated in coordinates of temperature and in-plane stress $\sigma_{\rho\rho}$. (c) Phase diagram of a freestanding BIT slab calculated in coordinates of temperature and in-plane stress $\sigma_{\rho\rho}$. PE is for paraelectric phase; FE is for ferroelectric phases with different polarization orientations (a, in plane; c, out of plane). $Q_{13} = -0.1$ m^4/C^2. (d) Dependence of in-plane ($P_{1,2}$) and out-of-plane (P_3) polarization components on in-plane stress $\sigma_{\rho\rho}$ for freestanding BIT slab (solid curves) and the film clamped on a rigid substrate (dashed curves). Temperature T = 25 °C. (e) BTFO phase diagram in coordinates of temperature−stress calculated for $Q_{13} = +0.3$ m^4/C^2. (f) Dependence of in-plane ($P_{1,2}$) and out-of-plane (P_3) polarization components on in-plane stress $\sigma_{\rho\rho}$ for BTFO film clamped on a rigid substrate (solid curves) and freestanding slab (dashed curves) calculated for T = 25 °C and $Q_{13} = +0.3$ m^4/C^2 (b).

The form of the LGD potential for both BTFO and BIT is given by

$$F_R \cong \alpha^*_1(P_1^2 + P_2^2) + \alpha^*_3 P_3^2 + \alpha^*_{33} P_3^4$$
$$+ \alpha^*_{13}(P_1^2 + P_2^2)P_3^2 + \alpha^*_{12}P_1^2 P_2^2 + \alpha^*_{11}(P_1^4 + P_2^4)$$
$$+ \alpha_{111}(P_1^6 + P_2^6) + \alpha_{333}P_3^6 + \alpha_{3333}P_3^8 \quad (2)$$

Here we suppose 4/mmm symmetry of the paraelectric phase of the bulk material. Coefficients $\alpha^*_1 = \alpha_1(T) - (Q_{11} + Q_{12})\sigma_{\rho\rho}$, $\alpha^*_3 = \alpha_3(T) - 2Q_{13}\sigma_{\rho\rho}$ are renormalized due to the in-plane stress $\sigma_{\rho\rho}$.[22] This renormalization primarily shifts the transition temperature between different ferroelectric phases, since $\alpha_i(T) = \alpha_i^T(T - T_{Ci}^{bulk})$.[23] The higher order LGD expansion coefficients for thin epitaxial films clamped on a rigid substrate are renormalized by electrostriction coupling as $\alpha^*_{11} = \alpha^\sigma_{11} + ((Q_{11}^2 + Q_{12}^2)s_{11} - 2Q_{11}Q_{12}s_{12})/(2(s_{11}^2 - s_{12}^2))$, $\alpha^*_{13} = \alpha^\sigma_{13} + Q_{13}(Q_{11} + Q_{12})/(s_{11} + s_{12})$, $\alpha^*_{33} = \alpha^\sigma_{33} + Q_{13}^2/(s_{11} + s_{12})$, and $\alpha^*_{12} = \alpha^\sigma_{12} - ((Q_{11}^2 + Q_{12}^2)s_{12} - 2Q_{11}Q_{12}s_{11})/(s_{11}^2 - s_{12}^2) + Q_{66}^2/(2s_{66})$. For the thick freestanding slab the coefficients are $\alpha^*_{11} = \alpha^\sigma_{11}$, $\alpha^*_{33} = \alpha^\sigma_{33}$, $\alpha^*_{12} = \alpha^\sigma_{12}$, and $\alpha^*_{13} = \alpha^\sigma_{13}$.

The calculated phase diagram in the coordinates of temperature vs radial stress $\sigma_{\rho\rho}$ is shown in Figure 5b for the films clamped on a rigid substrate and Figure 5c

for the freestanding BIT slabs. Dependencies of in-plane ($P_{1,2}$) and out-of-plane (P_3) polarization components on in-plane stress $\sigma_{\rho\rho}$ in BIT are shown in Figure 5d. As it follows from Figure 5d, in-plane polarization is evidently stronger than the out-of-plane component, and a tensile stress of more than +2 GPa is required to destroy P_3. Note that we see rather weak differences between the phase diagram and polarization values at temperatures lower than 500 °C for the freestanding slabs and clamped films. This is important; it is critical evidence that all observed effects originate from radial stresses imposed by the CFO inclusions, while the substrate influence is negligible. We also note that the vertical boundary between FEC and PE phases on the temperature−stress phase diagram is related to the independence of α_3 on temperature for the case of BIT, as obtained by Cross and Pohanka.[24] Using the BIT parameters as a guide, we calculated the BTFO phase diagram in coordinates of temperature vs radial stress $\sigma_{\rho\rho}$ and estimated the critical compressive stress σ_{cr} required for the appearance and stabilization of the out-of-plane polarization component in BTFO at room temperature as −0.2 GPa from Figure 5e. Since CFO inclusions are much stiffer than the BTFO matrix, it is natural to assume that they
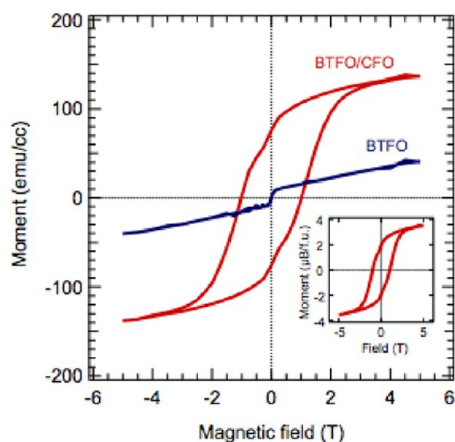
Figure 6. Set of in-plane $M–H$ curves measured at 10 K for BTFO and BTFO/CFO nanocomposite (30 vol % CFO). A strong magnetization with a hysteresis loop is found in the BTFO/CFO nanocomposite, but not in the pure BTFO. The magnetization arises from the CFO nanopillars, the saturation magnetization value of which is very close to that of the pure CFO film, ca. 4 μ_B/f.u., estimated by considering the volume fraction of CFO in the composite (inset).

indeed compress the matrix up to such (enough moderate) values. Overall Figure 5e for BTFO resembles BIT diagrams from Figure 5d, only shifted along the x-axis to negative (compressive) stresses. But in contrast to BIT, a compressive in-plane radial strain is critical for the stabilization of a weak out-of-plane polarization component (the aac-phase) in BTFO. Dependencies of in-plane ($P_{1,2}$) and out-of-plane (P_3) polarization components on in-plane stress $\sigma_{\rho\rho}$ in BTFO are shown in Figure 5f. As it follows from Figure 5f, out-of-plane polarization is evidently stronger than the in-plane component, at a compressive stress of more than -0.2 GPa. A tensile stress is required to destroy P_3 and stabilize the in-plane component $P_{1,2}$.

Having demonstrated polarization switching properties, attention is now paid to the magnetization behavior of this nanocomposite system. Figure 6 shows a set of in-plane $M–H$ curves measured at 10 K for BTFO and BTFO/CFO nanocomposite films. The BTFO/CFO nanocomposite exhibited a strong magnetization with a hysteresis loop that would originate from the ferro(i)magnetic nature of the nanocomposite, while almost no magnetization was observed for pure BTFO, although there are some claims of its having ferro(i)magnetism as well as ferroelectricity. Therefore most of magnetization of the nanocomposite film should arise from the CFO nanopillars; in fact, the saturation magnetization value is found to be very close to that of the pure CFO film, ca. 4 μ_B/f.u., estimated by considering the volume fraction of CFO in the composite (inset in Figure 6), and thus none of the CFO nanopillars embedded in BTFO were degraded in the magnetic property. The concurrent emergence of the out-of plane polarization of BTFO coupled with strong magnetic properties shown by the CFO indicates that the elastic coupling at the interface between CFO and BTFO could be systematically exploited to realize direction-dependent multiferroic properties. This is currently the focus of ongoing research and will be reported in the near future.

CONCLUSION

In summary we have shown a new bismuth-layered ferroelectric-spinel ferrite nanocomposite, namely, BTFO–CFO, grown epitaxially on (001) STO substrates. The CFO phase forms vertical nanopillars about 50 nm in diameter, irrespective of the volume fraction of CFO. HRTEM analyses show that the tubular interface between the nanopillars and the matrix is heavily strained and that the pillars are not perfectly vertical. This gives rise to a local shear, which is predicted to induce sufficient radial stresses that stabilize a weak out-of-plane and strong in-plane ferroelectric phase in the BTFO matrix. The saturation magnetization value is found to be very close to that of the pure CFO film, ca. 4 μ_B/f.u., estimated by considering the volume fraction of CFO in the composite, and thus no degradation in the magnetization values is observed.

METHODS

$Bi_4Ti_3O_{12}$ and CFO were selected as the starting materials. They were either simultaneously or alternatively deposited on 0.5 wt % Nb-doped $SrTiO_3$ (001) (Nb:STO) by pulsed laser deposition with total film thicknesses of 100 to 200 nm. The laser fluence and repetition rate were 2 J/cm^2 and 4$-$15 Hz depending on the deposition rate. The growth temperature was between 650 and 700 °C, and the oxygen partial pressure was 500 mTorr. The phase identification was made by X-ray diffraction and transmission electron microscopy with energy-dispersive X-ray spectroscopy analysis. The surface morphology of the films was observed by scanning electron microscopy and atomic force microscopy. The ferroelectric domain structure and polarization switching properties of the nanocomposite films were investigated using piezoresponse force microscopy. Details of the tip and imaging conditions are described in an earlier paper.[25] A superconducting quantum interference device (SQUID) was used to examine the magnetic property of the films.

REFERENCES AND NOTES

1. MacManus-Driscoll, J. L.; Zerrer, P.; Wang, H.; Yang, H.; Yoon, J.; Fouchet, A.; Yu, R.; Blamire, M. G.; Jia, Q. Strain Control and Spontaneous Phase Ordering in Vertical Nanocomposite Heteroepitaxial Thin Films. *Nat. Mater.* **2008**, *7*, 314–320.

2. Zheng, H.; Wang, J.; Lofland, S.; Ma, Z.; Mohaddes-Ardabili, L.; Zhao, T.; Salamanca-Riba, L.; Shinde, S.; Ogale, S.; Bai, F. Multiferroic $BaTiO_3$-$CoFe_2O_4$ Nanostructures. *Science* **2004**, *303*, 661–663.

3. Mohaddes-Ardabili, L.; Zheng, H.; Ogale, S.; Hannoyer, B.; Tian, W.; Wang, J.; Lofland, S.; Shinde, S.; Zhao, T.; Jia, Y. Self-Assembled Single-Crystal Ferromagnetic Iron Nanowires Formed by Decomposition. *Nat. Mater.* **2004**, *3*, 533–538.

4. Moshnyaga, V.; Damaschke, B.; Shapoval, O.; Belenchuk, A.; Faupel, J.; Lebedev, O.; Verbeeck, J.; van Tendeloo, G.; Muchsch, M.; Tsurkan, V. Structural Phase Transition at the Percolation Threshold in Epitaxial $(La_{0.7}Ca_{0.3}MnO_3)_{1-x}$:$(MgO)_x$ Nanocomposite Films. *Nat. Mater.* **2003**, *2*, 247–252.

5. Zavaliche, F.; Zhao, T.; Zheng, H.; Straub, F.; Cruz, M.; Yang, P.-L.; Hao, D.; Ramesh, R. Electrically Assisted Magnetic Recording in Multiferroic Nanostructures. *Nano Lett.* **2007**, *7*, 1586–1590.

6. Murakami, M.; Chang, K.-S.; Aronova, M.; Lin, C.-L.; Yu, M. H.; Simpers, J. H.; Wuttig, M.; Takeuchi, I.; Gao, C.; Hu, B. Tunable Multiferroic Properties in Nanocomposite $PbTiO_3$-$CoFe_2O_4$ Epitaxial Thin Films. *Appl. Phys. Lett.* **2005**, *87*, 112901-p1–112901-p3.

7. Béa, H.; Bibes, M.; Barthélémy, A.; Bouzehouane, K.; Jacquet, E.; Khodan, A.; Contour, J.-P.; Fusil, S.; Wyczisk, F.; Forget, A. Influence of Parasitic Phases on the Properties of $BiFeO_3$ Epitaxial Thin Films. *Appl. Phys. Lett.* **2005**, *87*, 072508-p1–072508-p3.

8. Ramesh, R.; Spaldin, N. A. Multiferroics: Progress and Prospects in Thin Films. *Nat. Mater.* **2007**, *6*, 21–29.

9. Cheong, S. W.; Mostovoy, M. Multiferroics: A Magnetic Twist for Ferroelectricity. *Nat. Mater.* **2007**, *6*, 13–20.

10. Schlom, D. G.; Ahn, C. H. Materials Science: Clear Leap for Superconductors. *Nature* **2008**, *456*, 582–583.

11. Alexe, M.; Ziese, M.; Hesse, D.; Esquinazi, P.; Yamauchi, K.; Fukushima, T.; Picozzi, S.; Gösele, U. Ferroelectric Switching in Multiferroic Magnetite (Fe_3O_4) Thin Films. *Adv. Mater.* **2009**, *21*, 4452–4455.

12. Zheng, H.; Zhan, Q.; Zavaliche, F.; Sherburne, M.; Straub, F.; Cruz, M. P.; Chen, L. Q.; Dahmen, U.; Ramesh, R. Controlling Self-Assembled Perovskite-Spinel Nanostructures. *Nano Lett.* **2006**, *6*, 1401–1407.

13. Liu, H. J.; Chen, L. Y.; He, Q.; Liang, C. W.; Chen, Y. Z.; Chien, Y. S.; Hsieh, Y. H.; Lin, S. J.; Arenholz, E.; Luo, C. W. Epitaxial Photostriction-Magnetostriction Coupled Self-Assembled Nanostructures. *ACS Nano* **2012**, *6*, 6952–6959.

14. De Araujo, C.-P.; Cuchiaro, J.; McMillan, L.; Scott, M.; Scott, J. Fatigue-Free Ferroelectric Capacitors with Platinum Electrodes. *Nature* **1995**, *374*, 627–629.

15. Park, B.; Kang, B.; Bu, S.; Noh, T.; Lee, J.; Jo, W. Lanthanum-Substituted Bismuth Titanate for Use in Non-Volatile Memories. *Nature* **1999**, *401*, 682–684.

16. Yang, H.; Wang, H.; Yoon, J.; Wang, Y.; Jain, M.; Feldmann, D. M.; Dowden, P. C.; MacManus-Driscoll, J. L.; Jia, Q. Vertical Interface Effect on the Physical Properties of Self-Assembled Nanocomposite Epitaxial Films. *Adv. Mater.* **2009**, *21*, 3794–3798.

17. Dix, N.; Muralidharan, R.; Guyonnet, J.; Warot-Fonrose, B.; Varela, M.; Paruch, P.; Sánchez, F.; Fontcuberta, J. On the

18. Hytch, M.; Snoeck, E.; Kilaas, R. Quantitative Measurement of Displacement and Strain Fields from HREM Micrographs. *Ultramicroscopy* **1998**, *74*, 131–146.

19. Rodriguez, B. J.; Jesse, S.; Baddorf, A. P.; Zhao, T.; Chu, Y. H.; Ramesh, R.; Eliseev, E. A.; Morozovska, A. N.; Kalinin, S. V. Spatially Resolved Mapping of Ferroelectric Switching Behavior in Self-Assembled Multiferroic Nanostructures: Strain, Size, and Interface Effects. *Nanotechnology* **2007**, *18*, 405701.

20. Nakashima, S.; Fujisawa, H.; Ichikawa, S.; Park, J. M.; Kanashima, T.; Okuyama, M.; Shimizu, M. Structural and Ferroelectric Properties of Epitaxial $Bi_5Ti_3FeO_{15}$ and Natural-Superlattice-Structured $Bi_4Ti_3O_{12}$-$Bi_5Ti_3FeO_{15}$ Thin Films. *J. Appl. Phys.* **2010**, *108*, 074106-p1–074106-p5.

21. Li, J. B.; Huang, Y. P.; Rao, G. H.; Liu, G. Y.; Luo, J.; Chen, J. R.; Liang, J. K. Ferroelectric Transition of Aurivillius Compounds $Bi_5Ti_3FeO_{15}$ and $Bi_6Ti_3Fe_2O_{18}$. *Appl. Phys. Lett.* **2010**, *96*, 222903-p1–222903-p3.

22. Pertsev, N. A.; Zembilgotov, A. G.; Tagantsev, A. K. Effect of Mechanical Boundary Conditions on Phase Diagrams of Epitaxial Ferroelectric Thin Films. *Phys. Rev. Lett.* **1998**, *80*, 1988.

23. Eliseev, E. A.; Morozovska, A. N. General Approach for the Description of Size Effects in Ferroelectric Nanosystems. *J. Mater. Sci.* **2009**, *44*, 5149–5160.

24. Cross, L. E.; Pohanka, R. C. Ferroelectricity in Bismuth Oxide Type Layer Structure Compounds. *Mater. Res. Bull.* **1971**, *6*, 939–949.

25. Imai, A.; Nagarajan, V.; Takahashi, R.; Lippmaa, M.; Matsumoto, Y. Self-Template Growth of Ferroelectric $Bi_4Ti_3O_{12}$ Nanoplates *via* Flux-Mediated Epitaxy with VO_x. *Cryst. Growth Des.* **2010**, *10*, 5233–5237.